Ti_3C_2 Mxene/porous g-C_3N_4 interfacial Schottky junction for boosting spatial charge separation in photocatalytic H_2O_2 production

Yang Yang[a,1], Zhuotong Zeng[b,1], Guangming Zeng[a,*], Danlian Huang[a,*], Rong Xiao[b,*], Chen Zhang[a], Chengyun Zhou[a], Weiping Xiong[a], Wenjun Wang[a], Min Cheng[a], Wenjing Xue[a], Hai Guo[a], Xiang Tang[a], Donghui He[a]

[a] College of Environmental Science and Engineering, Hunan University and Key Laboratory of Environmental Biology and Pollution Control, Ministry of Education (Hunan University), Changsha, 410082, PR China
[b] Department of Dermatology, Second Xiangya Hospital, Central South University, Changsha, 410011, PR China

ARTICLE INFO

ABSTRACT

The development of efficient photocatalysts for the production of hydrogen peroxide (H_2O_2) is a promising strategy to realize solar-to-chemical energy conversion. Graphitic carbon nitride (g-C_3N_4) presents giant potential for photocatalytic H_2O_2 production, but the sluggish charge separation depresses its photocatalytic performance. Herein, an interfacial Schottky junction composed of Ti_3C_2 nanosheets and porous g-C_3N_4 nanosheets (TC/pCN) is constructed by a facile electrostatic self-assembly route to significantly boost the spatial charge separation to promote the activation of molecular oxygen for H_2O_2 production. As the optimal sample, TC/pCN-2 possesses the highest H_2O_2 production rate ($2.20\,\mu mol\,L^{-1}\,min^{-1}$) under visible light irradiation ($\lambda > 420\,nm$), which is about 2.1 times than that of the porous g-C_3N_4. The results of superoxide radical detection and rotating disk electrode measurement suggest that the two-step single-electron reduction of oxygen is the predominant reaction step during this photocatalytic H_2O_2 production process. The enhanced photocatalytic performance is ascribed to the formation of Schottky junction and subsequent built-in electric field at their interface, which accelerate the spatial charge separation and restrain the charge recombination. This work provides an in-depth understanding of the mechanism of photocatalytic H_2O_2 production, and gives ideas for the design of highly active materials for photocatalytic H_2O_2 production.

1. Introduction

Hydrogen peroxide (H_2O_2) is a clean and multifunctional oxidant whose byproduct is only water [1,2]. It has been widely used in the field of chemical industry and environmental management, such as pulp bleaching, organic synthesis, disinfection, and water remediation [3–7]. Recently, H_2O_2 has also attracted tremendous interest as an ideal fuel cell energy carrier that can replace H_2 [8–10]. On the one hand, H_2O_2 can be stored and transported more conveniently and safely than that of H_2 due to its water solubility [11–13]. On the other, compared to two-compartment H_2 based fuel cell, the structure and scale of single-compartment direct peroxide-peroxide fuel cell (DPPFC) are more advanced [14,15]. However, the anthraquinone method as the most used method for H_2O_2 production is limited by its complicated routes, high costs, and toxic by-products [16]. Moreover, the synthesis of H_2O_2 in the presence of H_2 and O_2 though noble metal catalysts has the problem

of potentially explosive nature, and the method of obtaining H_2O_2 via electrocatalytic oxygen reduction reaction (ORR) is also restricted by its high energy consumption [17,18]. Therefore, the safe and efficient, environmental-friendly and low cost technology for H_2O_2 production is urgently desired [19–21].

As one of the most promising methods for H_2O_2 production, semiconductor photocatalysis owns the advantages of safety, pollution-free, and energy conservation [22–25]. In this process, photogenerated electrons on the conduction band originated from semiconductor materials can reduce O_2 to produce H_2O_2. Among the various semiconductor materials, graphitic carbon nitride (g-C_3N_4) has drawn much attentions owing to its efficient visible light absorption, proper conduction band edges, high chemical stability, and excellent environmental benignity [26–28]. Since Shiraishi et al. [29] firstly reported that g-C_3N_4 could highly selective produce H_2O_2 in an alcohol/water mixture with O_2 under visible light irradiation ($\lambda > 420\,nm$) due to

---

* Corresponding authors at: College of Environmental Science and Engineering, Hunan University, Changsha, 410082, PR China.
E-mail addresses: zgming@hnu.edu.cn (G. Zeng), huangdanlian@hnu.edu.cn (D. Huang), xiaorong65@csu.edu.cn (R. Xiao).
[1] These authors contribute equally to this article.

the efficient formation of 1,4-endoperoxide species, many investigations have been made in this field [30,31]. Nevertheless, the bulk g-C_3N_4 usually presents poor photocatalytic activity because of the low separation and transfer efficiency of photogenerated charge carriers. Therefore, various strategies have been developed for g-C_3N_4, such as defects engineering [32–34], heteroelements incorporating [35], and other species introducing [36,37], aiming at boosting the spatial charge separation, and thus improving the yield of H_2O_2 production.

Mxenes, a novel family of two-dimensional (2D) materials obtained by selectively etching the A layers from the MAX phases (M represents early transition metal, A represents A-group element, and X represents C and/or N element), have stimulated growing concerns recently [38,39]. Among them, Ti_3C_2 as a typical Mxene has been widely investigated since it was reported in 2011 because of its unique features, such as superior electrical conductivity, good structural stability, and excellent visible light harvesting ability [40]. Moreover, Ti_3C_2 could be combined with semiconductor photocatalysts to form Schottky junctions, which greatly promote the separation of photogenerated charge carriers. Thus, in addition to the bright future in the fields of Li-ion batteries and supercapacitors, Ti_3C_2 also presents great potentials in photocatalysis [41,42]. For example, Ran et al. [43] demonstrated that Ti_3C_2 could remarkably promote the photocatalytic H_2 production performance of CdS under visible light irradiation ($\lambda \geq 420$ nm). The H_2 production activity and the apparent quantum efficiency (AQE) of CdS/Ti_3C_2 hybrid photocatalyst could reach to 14,342 μmol h^{-1} g^{-1} and 40.1%, respectively, which could be ascribed to the excellent electrical conductivity, desirable Fermi level position and the formation of Schottky junction. Besides, Cao et al. [44] also found that the 2D/2D Ti_3C_2/Bi_2WO_6 heterostructure exhibited significantly enhanced activity toward photocatalytic CO_2 reduction. Benefiting from the improved charge transfer ability, the total yield of CH_4 and CH_3OH on Ti_3C_2/Bi_2WO_6 was 4.6 times than pristine Bi_2WO_6. These reports demonstrated that Ti_3C_2 could greatly promote the separation and transfer of photogenerated charge carriers, and thus improving the photocatalytic performance. Theoretically, when the metal's work function is greater than the n-type semiconductor's work function, a Schottky junction can be established after their intimate contact [45–47]. As the work function of Ti_3C_2 is greater than that of g-C_3N_4, it can be reasonably deduced that the interfacial Schottky junction composed of 2D Ti_3C_2 nanosheets and 2D porous g-C_3N_4 nanosheets might be a superior catalyst for photocatalysis, which may own enhanced visible light absorption, accelerated spatial charge separation, and a desirable yield of H_2O_2 [40,48].

In this study, a novel Ti_3C_2 Mxene/porous g-C_3N_4 (TC/pCN) interfacial Schottky junction is fabricated via a facile electrostatic self-assembly process. The performance of TC/pCN photocatalyst for H_2O_2 production under visible light irradiation ($\lambda > 420$ nm) is investigated. Based on the results of superoxide radical detection, rotating disk electrode measurement, photoelectrochemical properties and band structure analysis, the possible production mechanism of H_2O_2 over the TC/pCN photocatalyst is proposed. The introduction of Ti_3C_2 into g-C_3N_4 not only boosts the spatial charge separation, but also promotes the production of H_2O_2 under visible light.

2. Experimental section

2.1. Preparation of samples

2.1.1. Preparation of the porous g-C_3N_4 nanosheets

The porous g-C_3N_4 nanosheets were prepared by a chemical exfoliation method. Bulk g-C_3N_4 was first obtained by the thermal pyrolysis of urea on a semiclosed crucible at 520 °C for 2.5 h with a heating rate of 10 °C min^{-1}. Then 1 g of the bulk g-C_3N_4 was dispersed in 200 mL of 0.5 mol L^{-1} hydrochloric acid (HCl) solution under ultrasonic treatment. After ultrasonication for 1 h, the mixture was stirred for 4 h, then filtered and washed with deionized water until the pH $\geq$ 6.

Finally, the porous g-C_3N_4 nanosheets were obtained by drying the product at 60 °C for 12 h.

2.1.2. Preparation of the Ti_3C_2 nanosheets

The Ti_3C_2 nanosheets were prepared according to the previous report [44]. Typically, 1 g of Ti_3AlC_2 was dispersed in 20 mL of hydrofluoric acid (HF) solution (content $\geq$ 40.0%). After stirring for 72 h, the suspension was centrifuged, washed with deionized water until the pH $\geq$ 6, and dried for 8 h under vacuum at 60 °C. Then, the precursor was added into 20 mL of dimethyl sulfoxide (DMSO) and kept stirring for 12 h. The mixture was centrifuged, washed with deionized water for several times to remove the remainder DMSO, and dried for 8 h under vacuum at 60 °C. Subsequently, 0.5 g of the dried sample was dispersed in 50 mL of deionized water and ultrasound-treated for 1 h under N_2 protection followed by 1 h of centrifugation at 3500 rpm to remove the unexfoliated sample. Finally, the supernatant of Ti_3C_2 nanosheets was obtained, and its concentration was measured to be 1 mg mL^{-1}.

2.1.3. Preparation of the Ti_3C_2/porous g-C_3N_4 (TC/pCN) sample

The Ti_3C_2/porous g-C_3N_4 (TC/pCN) sample was prepared by a facile electrostatic self-assembly method. Typically, 0.3 g of the porous g-C_3N_4 was dispersed in 50 mL of deionized water and ultrasound-treated for 0.5 h. Subsequently, a certain volume of the Ti_3C_2 solution was added dropwise into the above suspension and ultrasound-treated for another 0.5 h to delaminate and strengthen the interfacial interaction. The mixture was then stirred for 4 h to build the mutual electrostatic attraction between the two species. Finally, the precipitate was filtered and dried for 8 h under vacuum at 60 °C. The mass ratios of Ti_3C_2 to porous g-C_3N_4 were set as 1%, 2%, and 5% by controlling the added volume of Ti_3C_2 solution, and the obtained samples were designated as TC/pCN-X (X = 1, 2, 5). The porous g-C_3N_4 with no Ti_3C_2 solution adding was defined as pCN.

2.2. Characterization

Zeta potential was detected by a Zetasizer Nano ZS (Malvern, UK). Transmission electron microscopy (TEM) images were collected on a Tecnai G2 F20 S-TWIN electron microscope (FEI, USA). Atomic force microscopy (AFM) images were acquired on a Dimension Edge (Bruke, Germany). Energy-dispersive X-ray spectroscopy (EDS) mapping images were obtained on a Quanta 250 field emission scanning electron microscopy (FESEM, FEI, USA). Brunauer-Emmett-Teller (BET) specific surface areas were measured by N_2 adsorption-desorption method using an ASAP 2020 HD88 instrument (Micromeritics, USA). X-ray diffraction (XRD) patterns were tested on a D8 Advance X-ray diffractometer (Bruke, Germany) with Cu Kα radiation. Fourier transform infrared (FTIR) spectra were monitored using a KBr pellet on a TENSOR 27 spectrometer (Bruke, Germany). Ultraviolet visible diffuse reflectance spectra (UV–vis DRS) were measured on a Cary 300 spectrophotometer (Varian, USA). X-ray photoelectron spectroscopy (XPS) was performed on a Escalab 250Xi spectrometer (Thermo, USA) with Al Kα radiation. Photoluminescence (PL) spectra were conducted on a F-7000 fluorescence spectrophotometer (Hitachi, Japan) under 320 nm excitation. Time-resolved photoluminescence (TRPL) spectra were recorded on a FLS 980 fluorescence spectrophotometer (Edinburgh Instruments, UK). Ultraviolet photoemission spectroscopy (UPS) was carried out on a Escalab 250Xi spectrometer (Thermo, USA) using He I resonance lines (21.2 eV).

2.3. Photocatalytic H_2O_2 production

The photocatalytic H_2O_2 production experiments were carried out as follows. First, 50 mg of catalyst powder was uniformly dispersed into 50 mL of aqueous solution containing 10 vol% isopropanol (IPA) with ultrasonication for 10 min. Then O_2 was continually bubbled through the suspension and stirred in the dark for 1 h to achieve the adsorption-

desorption equilibrium before irradiation. Finally, the suspension was irradiated with a 300 W xenon lamp (PLS-SXE300/300UV, Perfect Light, China) equipped with a 420 nm cutoff filter under stirring. At certain time intervals, 3 mL of the suspension was collected. After removing the catalyst powder by centrifugation and filtration with a millipore filter (0.45 μm), the H_2O_2 concentration was measured by iodometry [30]. The H_2O_2 decomposition behavior of the photocatalysts was studied by dispersing 50 mg of sample in 50 mL of 1 mmol L^{-1} H_2O_2 solution and irradiating for 1 h visible light under continuous stirring. To evaluate the stability and recyclability of the photocatalysts, after reaction, the samples were collected by centrifugation and washed with deionized water and ethanol respectively, and dried for the cycle experiments.

2.4. Superoxide radical detection

The electron spin response (ESR) signal of $\cdot O_2^-$ was obtained from a JEOL JES-FA200 spectrometer under visible light irradiation ($\lambda > 420$ nm), where 5,5-dimethyl-1-pyrroline N-oxide (DMPO) was used as spin-trapped reagent. The concentration of $\cdot O_2^-$ was evaluated by nitroblue tetrazolium (NBT) transformation test, in which 50 mg of the sample was dispersed in 50 mL of 0.01 mmol L^{-1} NBT aqueous solution. NBT concentration was measured by a Shimadzu UV-2700 spectrophotometer at its characteristic absorbance peak (260 nm).

2.5. Electrochemical and photoelectrochemical measurement

Rotating disk electrode (RDE) measurement was conducted on a Chenhua CHI 760E electrochemical workstation with a three-electrode cell. The Ag/AgCl electrode and Pt wire electrode were used as the reference electrode and counter electrode, respectively. The working electrode was prepared as follows: 5 mg of the sample was added into 0.5 mL of 10 vol% Nafion solution (diluted with ethanol). Then 5 μL of the suspension was uniformly dropped on a glassy carbon electrode (diameter of 5 mm) and the electrode was dried at room temperature. The linear sweep voltammetry (LSV) curves were collected in an O_2-saturated 0.1 mmol L^{-1} phosphate buffer solution (pH 7) with a scan rate of 10 mV s^{-1}.

The transient photocurrent response curves, electrochemical impedance spectroscopy (EIS) and Mott-Schottky plots were obtained on a Chenhua CHI 760E electrochemical workstation with a three-electrode cell. The Ag/AgCl electrode and Pt wire electrode were used as the reference electrode and counter electrode, respectively. The working electrode was prepared as follows: 5 mg of the sample was added into 1 mL of 0.5% nafion solution under ultrasonication for 1 h. The suspension was then dropped on a fluorine-doped tinoxide (FTO) glass (1×2 cm^2) which was pre-cleaned by acetone, ethanol and deionized water, respectively. The obtained electrode was dried at 80 °C for 4 h and calcined at 120 °C for 1 h. 0.2 mmol L^{-1} Na_2SO_4 aqueous solution was used as the electrolyte. The light source was provided by a 300 W xenon lamp (PLS-SXE300/300UV, Perfect Light, China) equipped with a 420 nm cutoff filter. The transient photocurrent response was tested on an applied voltage of 0 V with the light on or off. The electrochemical impedance spectroscopy (EIS) was collected on an applied voltage of 0 V with an amplitude of 0.005 V over a frequency between 10^{-2} and 10^5 Hz. Moreover, Mott-Schottky curves were also collected at the frequency of 1000 Hz.

3. Results and discussion

3.1. Synthesis and physicochemical properties

Fig. 1 displays the synthetic process of TC/pCN interfacial Schottky junction. Initially, Ti_3AlC_2 MAX phase was etched into multilayer Ti_3C_2 by HF. The multilayer Ti_3C_2 was subsequently exfoliated into few-layer ultrathin Ti_3C_2 nanosheets under a DMSO assisted ultrasonication.

Meanwhile, the porous $g-C_3N_4$ was obtained from the delamination of bulk $g-C_3N_4$ by HCl assisted ultrasonication. Zeta potential analysis shows that the potential of Ti_3C_2 (Fig. S1a) and porous $g-C_3N_4$ (Fig. S1b) surface is negative (-27 mV) and positive (21 mV), respectively. Thus, the spontaneous self-assembly between the positively charged porous $g-C_3N_4$ and the negatively charged Ti_3C_2 was realized by the electrostatic interaction.

The morphology and microstructure of the samples were characterized by TEM. As displayed in Fig. 2a, the Ti_3C_2 nanosheets are almost transparent, indicating the existence of ultrathin nanostructure. The darker color is observed in some place, which can be ascribed to the crumple of highly flexible Ti_3C_2 nanosheets [49]. As for $g-C_3N_4$ (Fig. 2b), it presents typical sheet-like and porous morphology. Meanwhile, it can be clearly seen from Fig. 2c that the TC/pCN-2 possesses 2D nanostructure consisted of Ti_3C_2 nanosheets and porous $g-C_3N_4$ nanosheets. And because of the electrostatic attraction between the two parts, their contact is quite intimate. Moreover, high-resolution TEM (HRTEM) was performed to obtain more information about the two species. From Fig. 2d, no clear fringe can be observed in the part of porous $g-C_3N_4$ due to its low crystallinity, whereas an obvious lattice fringe with the measured spacing of 0.264 nm can be found in Ti_3C_2, which is in good agreement with the (010) crystal plane of Ti_3C_2 [41]. Besides, AFM image (Fig. 2e) and the corresponding height distribution profile (Fig. 2f) show that the TC/pCN-2 possesses typical 2D hierarchical nanostructure. Additionally, FESEM-EDS elemental mapping was collected to further authenticate the presence of the hybridization. As shown in Fig. 2g, the elements of C, N, Ti, F and O distribute across the TC/pCN-2 uniformly, and no other foreign elements can be detected, thereby validating the elemental composition of the sample qualitatively. Therefore, these results demonstrate the successful assembly of Ti_3C_2 nanosheets with porous $g-C_3N_4$ nanosheets for TC/pCN-2 interfacial Schottky junction. The BET specific surface area of the samples were analyzed by N_2 adsorption-desorption isotherms shown in Fig. S2. The BET specific surface area of the pCN, TC/pCN-1, TC/pCN-2, TC/pCN-5 and Ti_3C_2 samples are 52.37, 54.70, 59.34, 56.37 and 8.45 m^2 g^{-1}, respectively. As the content of Ti_3C_2 increases, the specific surface area of the composite gradually increases and the TC/pCN-2 sample has the largest surface area. With further increasing the Ti_3C_2 content, the specific surface area of the composite decreases because of the relatively small surface area of Ti_3C_2.

The crystal structure of the samples was analyzed by XRD. The sample with intense peaks in Fig. 3a can be assigned to MAX phase Ti_3AlC_2. After HF etching treatment, the diffraction peaks of (002) and (004) shift to lower degrees and the most intense diffraction peak at 39.0° disappears, suggesting the removal of Al element in Ti_3AlC_2 and successful transformation of Ti_3AlC_2 to Ti_3C_2 [41]. Meanwhile, most of the peaks in Ti_3C_2 become weaker and broader compared to Ti_3AlC_2, which is ascribed to the thinner layered structure of Ti_3C_2. Fig. 3b displays the XRD patterns of TC/pCN samples with different Ti_3C_2 contents. All of the samples present two similar diffraction peaks. The peak (002) at 27.5° is indexed to the stacking reflection of conjugated planes, and the other peak (110) at 13.1° represents the repetition of nonplanar units [50]. No distinct diffraction peaks of Ti_3C_2 can be detected, indicating the well distribution and limited amount of Ti_3C_2 in the TC/pCN samples. Fig. 3c shows FTIR spectra of the samples. No clear peaks can be observed in the Ti_3C_2 and the framework of TC/pCN is similar to that of $g-C_3N_4$, suggesting that the signals in TC/pCN are from $g-C_3N_4$. Specifically, the peak around 810 cm^{-1} is ascribed to the breathing vibration of triazine units, and the peaks between 1200 and 1700 cm^{-1} are assigned to the skeletal stretching of C–N heterocycles [51,52]. Additionally, the peaks between 3000 and 3400 cm^{-1} belong to the -NH and $-$OH stretching vibrations because of the free amino groups and adsorbed hydroxyl species [53,54]. The optical absorption properties of the samples were studied by UV–vis DRS. As displayed in Fig. 3d, pristine porous $g-C_3N_4$ exhibits an absorption band around 450 nm. The bare Ti_3C_2 presents a broad and intense absorption from

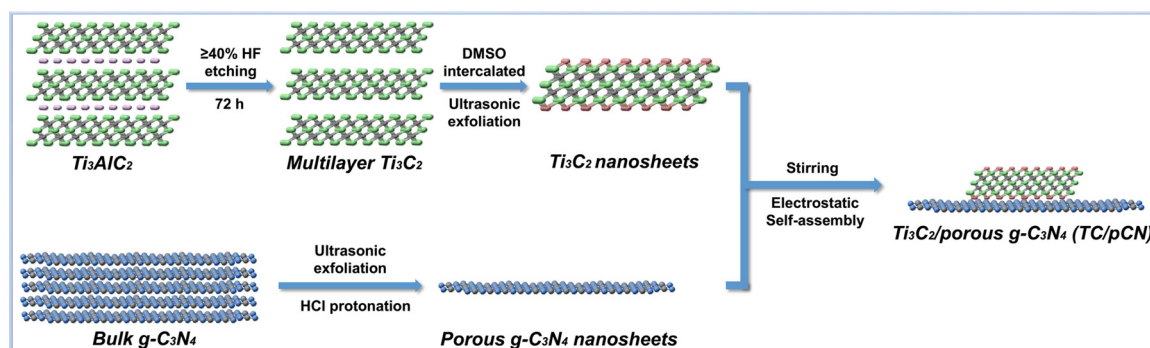**Fig. 1.** Schematic illustration of synthetic process of Ti$_3$C$_2$/porous g-C$_3$N$_4$ (TC/pCN) interfacial Schottky junction.
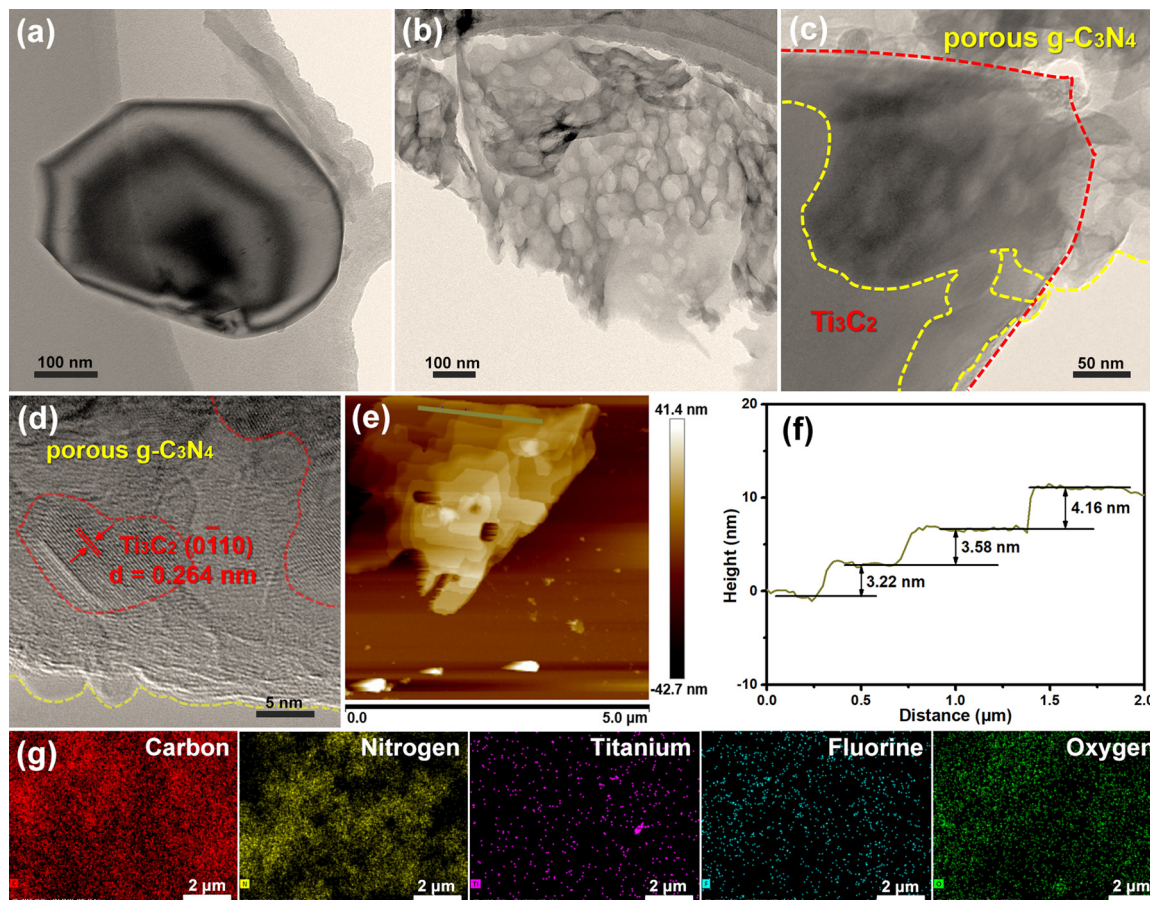

Fig. 2. TEM images of (a) Ti$_3$C$_2$, (b) pCN and (c) TC/pCN-2; (d) HRTEM image, (e) AFM image and (f) the corresponding height distribution profile, and (g) FESEM-EDS elemental mapping of TC/pCN-2.

300 to 800 nm. After hybridizing porous g-C$_3$N$_4$ with Ti$_3$C$_2$, the visible-light harvesting ability is significantly enhanced. The absorbance in the visible light region of the TC/pCN becomes stronger as the content of Ti$_3$C$_2$ increases. These changes are further evidenced by the physical appearance changes. As shown in the insert image of Fig. 3d, the color of the sample change from bright yellow to dark yellow with the increase of Ti$_3$C$_2$ content.

The surface chemical composition and states of the samples were investigated by XPS. As displayed in the XPS survey spectra (Fig. 4a), C, N and O elements related to g-C$_3$N$_4$ can be seen in TC/pCN-2, while Ti and F elements related to Ti$_3$C$_2$ cannot be clearly observed due to their weak intensity. The presence of Ti and F elements in TC/pCN-2 are further verified by the high-resolution spectra, demonstrating that the Ti$_3$C$_2$ are successfully incorporated into the g-C$_3$N$_4$. Fig. 4b shows the high-resolution Ti 2p spectra of Ti$_3$C$_2$ and TC/pCN-2. The Ti 2p

spectrum of Ti$_3$C$_2$ are deconvoluted into five peaks, in which 455.3 and 461.3 eV can be assigned to Ti-C, 457.3 and 463.2 eV is related to Ti-O, and 459.3 eV belongs to Ti-F [44]. Compared to Ti$_3$C$_2$, the binding energies of all Ti-related peaks in TC/pCN-2 exhibit a negative shift. The high-resolution F 1 s spectra of Ti$_3$C$_2$ and TC/pCN-2 are provided in Fig. 4c. For Ti$_3$C$_2$, two peaks at 684.9 and 689.8 eV can be detected, corresponding to F-Ti and F-C, respectively [43]. In comparison with the F 1 s spectrum of Ti$_3$C$_2$, the binding energies in TC/pCN-2 also show a negative shift. In addition, Fig. 4d displays the high-resolution C 1s spectra of the samples. All the binding energies at 284.8 eV are ascribed to C-C (adventitious carbon) [50]. Ti$_3$C$_2$ presents three characteristic peaks at 281.8, 286.3 and 288.9 eV, which are attributed to the C—Ti, C—O and C—F, respectively [44]. As for TC/pCN-2, the binding energy of C 1s in 285.8 and 288.4 are assigned to the C—N and C—N=C [55], which exhibits a positive shift in comparison with that in the g-C$_3$N$_4$.
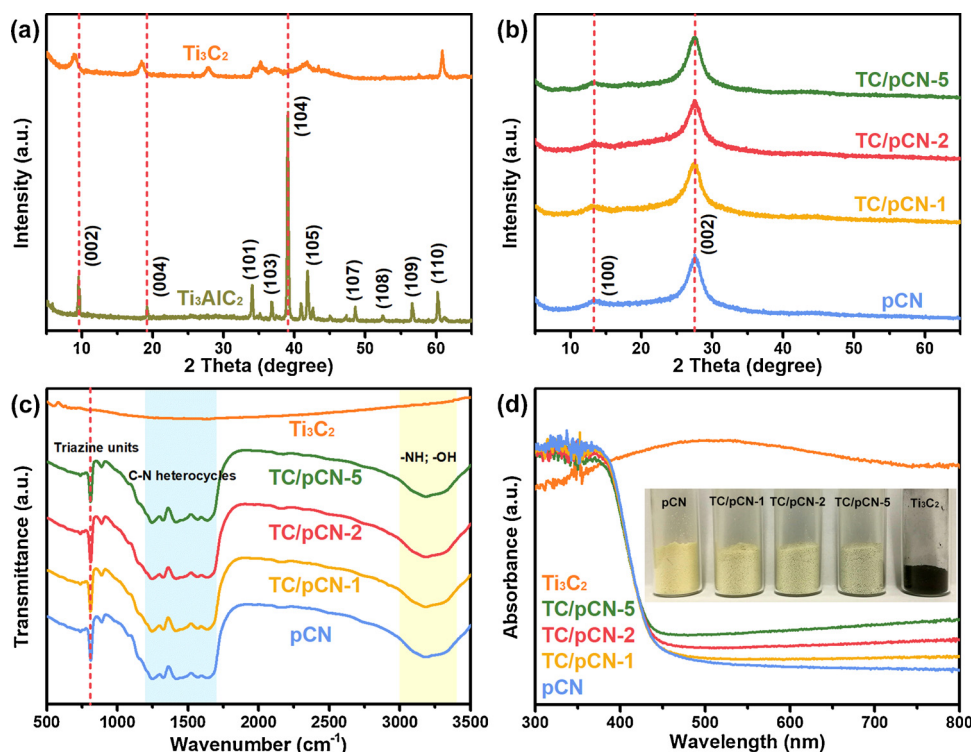
Fig. 3. (a) XRD patterns of Ti$_3$AlC$_2$ and Ti$_3$C$_2$; (b) XRD patterns of pCN and TC/pCN samples; (c) FTIR spectra of the samples; (d) UV–vis DRS spectra and a photograph (inset) of the samples.

No obvious C-Ti can be detected in TC/pCN-2 because of the limited content of Ti$_3$C$_2$. Fig. 4e demonstrates that the O 1s region of Ti$_3$C$_2$ can be divided into three species (O-Ti, OH-Ti and adsorbed H$_2$O or CO$_2$) [44], which are located at 529.6, 530.8 and 531.8 eV, respectively. Only peak about adsorbed H$_2$O or CO$_2$ can be obviously found in TC/pCN-2. Besides, TC/pCN-2 presents N 1s spectrum similar to pCN, as shown in Fig. 4f, the peaks located at 398.9, 399.9, 401.2 and 404.2 eV are related to C–N=C, N-C$_3$, C–NH and charging effects in heterocycles, respectively [56]. These changes demonstrate that electrons transfer from g-C$_3$N$_4$ to Ti$_3$C$_2$ in the TC/pCN-2 sample due to the strong Schottky effect between the g-C$_3$N$_4$ and Ti$_3$C$_2$, increasing the electron density of Ti$_3$C$_2$.

3.2. Spatial charge separation ability

The spatial charge separation ability of the TC/pCN interfacial Schottky junction during the photocatalysis was investigated. Fig. 5a displays the transient photocurrent response curves of the samples on typical cycles of visible light irradiation on or off, which directly interrelates with their spatial charge separation ability [57–59]. With the light on, the current is generated immediately, demonstrating the high photo-sensitivity and efficient spatial charge separation of the samples. Compared to pCN, all the TC/pCN-X (X = 1, 2, 5) samples show elevated photocurrent response, and TC/pCN-2 presents the maximum photocurrent density, indicating that the Ti$_3$C$_2$ can greatly accelerate the spatial charge separation on the samples. Moreover, the spatial charge separation efficiency of the samples was examined by the PL technique [60,61]. As shown in Fig. 5b, a broad PL band (425–550 nm) with a peak at 465 nm is observed on pCN, which can be ascribed to the radiative recombination of electron-hole pairs. The introduction of Ti$_3$C$_2$ leads to substantial suppression of radiative electron-hole recombination in g-C$_3$N$_4$. The TC/pCN-2 presents the weakest PL intensity, implying the fastest spatial charge separation [62,63]. To get more information about spatial charge separation and transfer, TRPL test were conducted. As shown in Fig. 5c, the fluorescence decay curves

can be fitted by a biexponential model (Eq. (1)):

$$R(t) = B_1\exp(-t/\tau_1) + B_2\exp(-t/\tau_2) \tag{1}$$

Where B_1 and B_2 are the weight factor, and τ_1 and τ_2 are the short and long fluorescent lifetime, respectively. Clearly, both the short and long lifetimes of TC/pCN-2 (τ_1 = 2.75 ns, 41.09%; τ_2 = 10.52 ns, 58.91%) are prolonged in comparison with those of pCN (τ_1 = 2.51 ns, 37.01%; τ_2 = 9.12 ns, 62.99%). Therefore, the average fluorescent lifetime (Ave.τ) is calculated via the following Eq. (2):

$$\tau_{ave} = \frac{B_1\tau_1^2 + B_2\tau_2^2}{B_1\tau_1 + B_2\tau_2} \tag{2}$$

and the average fluorescent lifetime increases from 8.20 ns (pCN) to 9.32 ns (TC/pCN-2), demonstrating that the incorporation of Ti$_3$C$_2$ on g-C$_3$N$_4$ can efficiently accelerate the spatial charge separation and depress the charge recombination, and thus elongate the lifetime of photogenerated charge carriers [43,57]. EIS are employed to reflect the electronic conductivity and the interfacial charge transfer behavior of the samples [64,65]. As displayed in Fig. 5d, TC/pCN-2 presents an obvious decrease in the semicircle diameters compared with that of pCN, implying that the TC/pCN-2 interface has a better electrical conductivity, which is beneficial for achieving efficient spatial charge separation and transfer during the photocatalytic process.

3.3. Photocatalytic H$_2$O$_2$ production

The photocatalytic H$_2$O$_2$ production ability of the TC/pCN interfacial Schottky junction was evaluated by O$_2$ reduction from isopropanol solution under visible light irradiation (λ > 420 nm). As shown in Fig. 6a, the yield of H$_2$O$_2$ is distinctly increased by compounding Ti$_3$C$_2$ with porous g-C$_3$N$_4$. The TC/pCN-2 presents the best photocatalytic performance, the amount of H$_2$O$_2$ (131.71 μmol L^{-1}) produced after 60 min of visible light irradiation is about 2.1 times than that of the pCN (61.63 μmol L^{-1}). Fig. S3 displays the UV–vis absorption spectrum changes on TC/pCN-2 among the H$_2$O$_2$ production
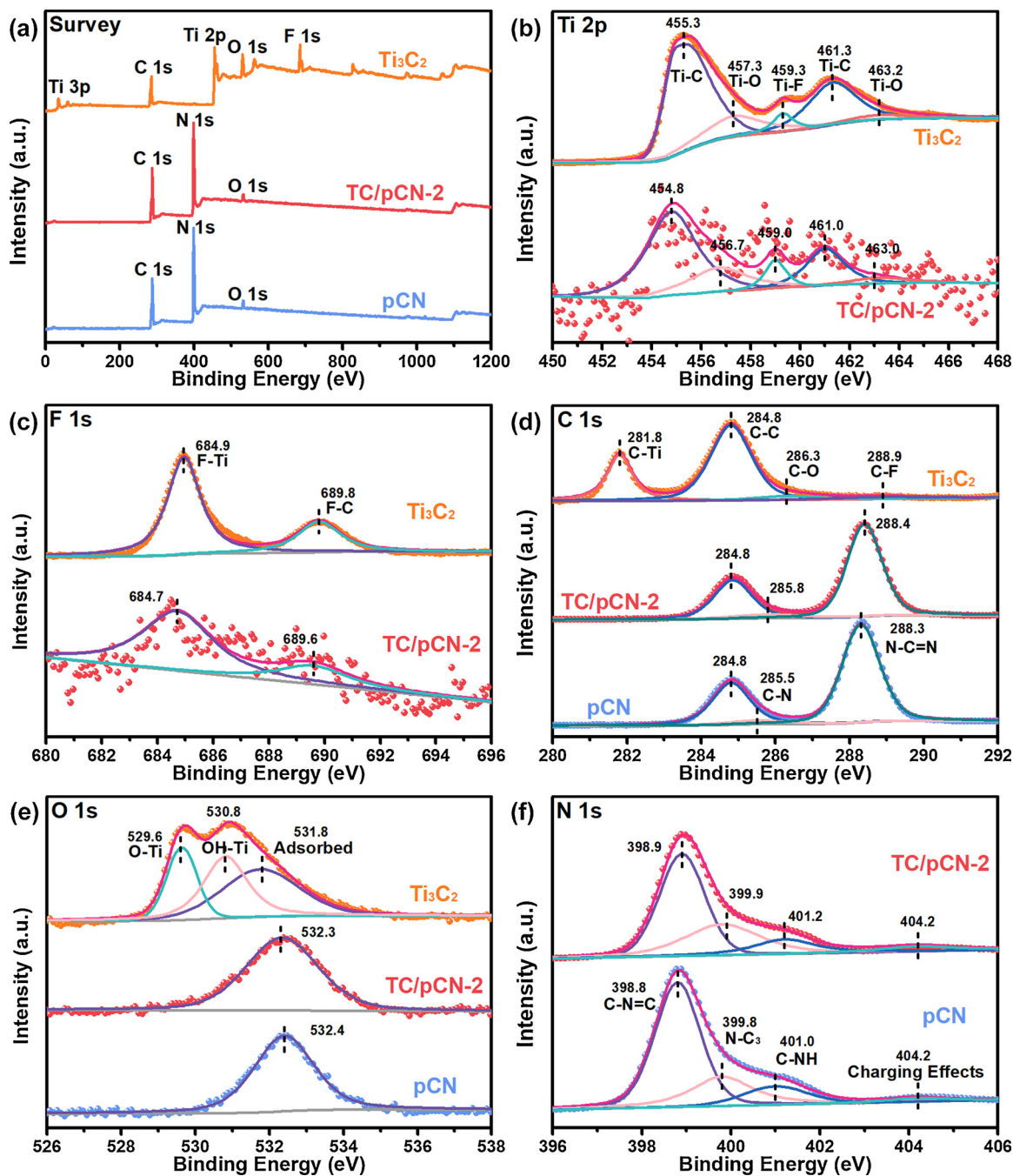
Fig. 4. XPS spectra of Ti$_3$C$_2$, pCN and TC/pCN-2: (a) total survey, (b) Ti 2 p, (c) F 1 s, (d) C 1 s, (e) O 1s and (f) N 1s.

process. It can be clearly observed that the absorbance at 350 nm significantly increases with the prolongation of irradiation time. However, when the mass ratio of Ti$_3$C$_2$ to porous g-C$_3$N$_4$ is excessive (TC/pCN-5), the yield of H$_2$O$_2$ decreases presumably because of the light shielding effect. Meanwhile, control experiments reveal that H$_2$O$_2$ can hardly be detected in the absence of photocatalyst or only in the presence of Ti$_3$C$_2$, indicating the decisive role of photocatalysis in the H$_2$O$_2$ production process.

In the process of photocatalytic H$_2$O$_2$ production, the formation and decomposition of H$_2$O$_2$ exist simultaneously since H$_2$O$_2$ can be decomposed by photogenerated charge carriers. Therefore, the zero-order kinetic (H$_2$O$_2$ formation) and first-order kinetic (H$_2$O$_2$ decomposition) are utilized to evaluate the behavior of H$_2$O$_2$ production. The kinetic model shown in Eq. (3) provides the H$_2$O$_2$ concentration as a function of reaction time [66].

$$[H_2O_2] = \frac{K_f}{K_d}(1 - \exp(-K_d t)) \tag{3}$$

K_f and K_d are the formation rate constant (µmol L^{-1} min^{-1}) and decomposition rate constant (min^{-1}), respectively. The values of K_f and K_d are estimated by fitting the data in Fig. 6a into Eq. (3) and the results are displayed in Fig. 6b. The K_f value significantly increases by the introduction of Ti$_3$C$_2$, reaching a maximum at TC/pCN-2 which is approximately 2.1 times than pCN (from 1.12 to 2.38 µmol L^{-1} min^{-1}), while the K_d value of TC/pCN-2 (2.38 × 10^{-3} min^{-1}) is smaller than that of pCN (2.65 × 10^{-3} min^{-1}). The positive effect of Ti$_3$C$_2$ on the K_f is well matched with the overall H$_2$O$_2$ production. These results demonstrate that the combination of porous g-C$_3$N$_4$ with Ti$_3$C$_2$ can promote the formation of H$_2$O$_2$ and depress decomposition of H$_2$O$_2$.

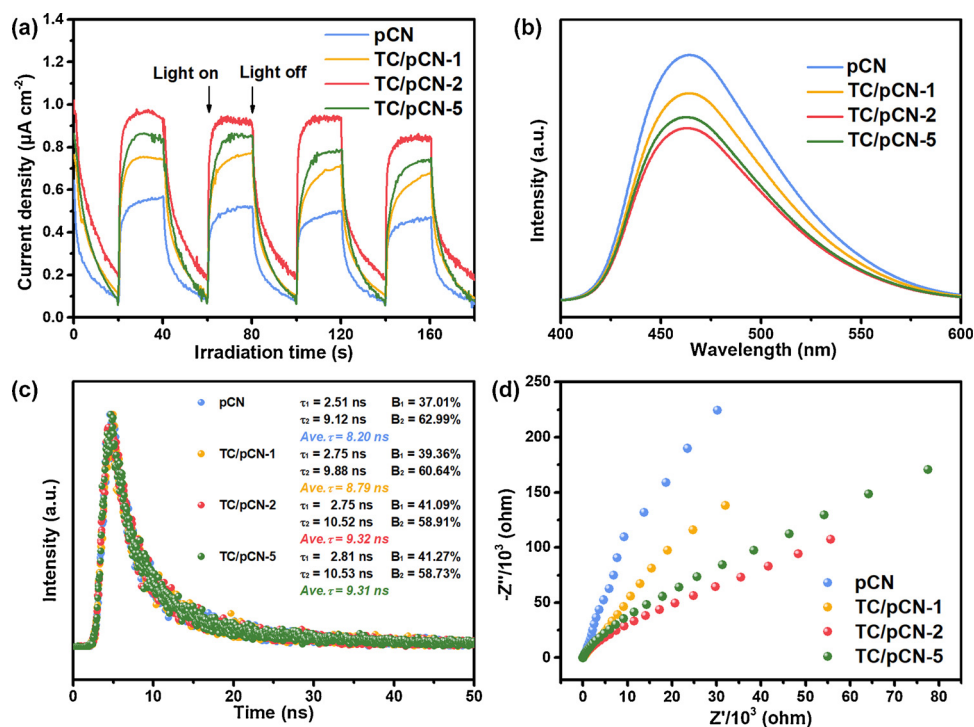To further investigate the decomposition behavior of H$_2$O$_2$ in the

Fig. 5. (a) Transient photocurrent response curves, (b) PL spectra, (c) TRPL spectra and (d) EIS Nyquist plots of the samples.
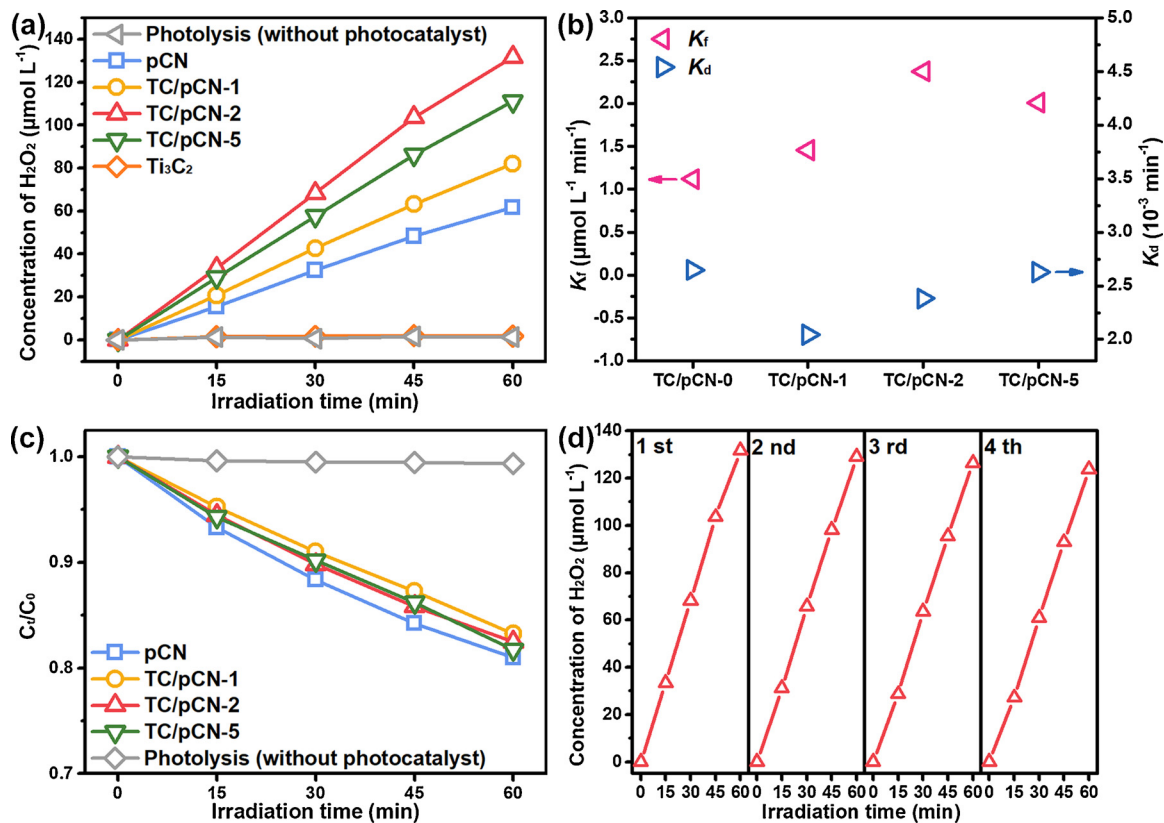

Fig. 6. (a) Time-dependent production of H_2O_2 under visible light irradiation; (b) Formation rate constant (K_f) and decomposition rate constant (K_d) for H_2O_2 production; (c) The photocatalytic decomposition of H_2O_2 (1 mmol L^{-1}) under visible light irradiation; (d) Cycling runs for the photocatalytic H_2O_2 production over TC/pCN-2.

Table 1
Comparison with other g-C$_3$N$_4$ based photocatalysts for H$_2$O$_2$ production.

Photocatalysts	Dosage (g L^{-1})	Reaction solution	Light source	H$_2$O$_2$ production activity (µmol g^{-1} h^{-1})	Ref.
g-C$_3$N$_4$/PDI	1.67	Water (30 mL)	2 kW XL (λ > 420 nm)	21.08	[36]
g-C$_3$N$_4$/PDI/rGO	1.67	Water (30 mL)	2 kW XL (λ > 420 nm)	24.17	[37]
3DOM g-C$_3$N$_4$-PW$_{11}$	1.00	Water (100 mL)	300 W XL (λ > 320 nm)	35.00	[14]
Ag@U-g-C$_3$N$_4$-NS	1.00	Water (100 mL)	300 W XL (λ > 320 nm)	≈ 67.50	[31]
g-C$_3$N$_4$-CoWO	1.00	Water (100 mL)	300 W XL (λ ≥ 420 nm)	97.00	[12]
g-C$_3$N$_4$-CNTs	1.00	10 vol% FA (100 mL)	300 W XL (λ ≥ 400 nm)	487.00	[9]
g-C$_3$N$_4$	4.00	90 vol% EA (5 mL)	2 kW XL (λ > 420 nm)	125.00	[29]
Mesoporous g-C$_3$N$_4$	4.00	90 vol% EA (5 mL)	2 kW XL (λ > 420 nm)	≈ 183.50	[32]
KPD-CN	0.50	10 vol% EA (40 mL)	300 W XL (λ ≥ 420 nm)	≈ 485.50	[35]
DCN	0.83	20 vol% IPA (60 mL)	AM1.5 (λ > 420 nm)	96.80	[33]
OCN	1.00	10 vol% IPA (50 mL)	300 W XL (λ > 420 nm)	1200.00	[30]
Ti$_3$C$_2$/porous g-C$_3$N$_4$	1.00	10 vol% IPA (50 mL)	300 W XL (λ > 420 nm)	131.71	This work

PDI: pyromellitic diimide; rGO: reduced graphene oxide; 3DOM g-C$_3$N$_4$: three dimensionally ordered macroporous graphitic carbon nitride; PW$_{11}$: polyoxometalate (POMs) cluster of [PW$_{11}$O$_{39}$]$^{7-}$; U-g-C$_3$N$_4$-NS: ultrathin g-C$_3$N$_4$ nanosheets; CoWO: POMs-derived metal oxides; CNTs: carbon nanotubes; KPD-CN: (K, P, and O)-incorporated polymeric carbon nitride; DCN: defective g-C$_3$N$_4$; OCNs: oxygen-enriched carbon nitride polymer; FA: formic acid; EA: ethanol; IPA: isopropanol; XL: Xenon lamp.

presence of photocatalysts under visible light irradiation, the H$_2$O$_2$ decomposition experiments were performed with an initial H$_2$O$_2$ concentration of 1 mmol L^{-1}. As exhibited in Fig. 6c, the H$_2$O$_2$ decomposes about 17.5% on TC/pCN-2 after 60 min of visible light irradiation, which is lower than that on pCN (19.0%). In the absence of photocatalysts, the decomposition of H$_2$O$_2$ is negligible. The decomposition rate constant (K_d') are estimated by the following Eq. (4):

$$K_d' = \frac{-\ln(C_t/C_0)}{t} \qquad (4)$$

Where C_t is the H$_2$O$_2$ concentration at time t, C_0 is the initial concentration of H$_2$O$_2$ (1 mmol L^{-1}). The results in Fig. S4 illustrate that the K_d' value of TC/pCN-2 (3.21 × 10^{-3} min^{-1}) is smaller than that of pCN (3.49 × 10^{-3} min^{-1}). The results further confirm the inhibition of H$_2$O$_2$ decomposition in the TC/pCN-2, which will elevate the yield of H$_2$O$_2$ production.

Besides, the recyclability and physicochemical stability of the TC/pCN-2 in the photocatalytic H$_2$O$_2$ production were also investigated. The cyclic experiments were conducted and the results are exhibited in Fig. 6d. Obviously, the yield of H$_2$O$_2$ can still reach to 123.83 µmol L^{-1} after four consecutive cycles. The physicochemical properties of the TC/pCN-2 after photocatalytic H$_2$O$_2$ production for four times were further characterized by the XRD (Fig. S5), FTIR (Fig. S6) and XPS (Fig. S7) techniques, and no obvious changes can be seen, demonstrating that the photocatalyst is stable. Moreover, the H$_2$O$_2$ production activity of TC/pCN-2 (131.71 µmol g^{-1} h^{-1}) is higher than most of other g-C$_3$N$_4$-based photocatalysts reported previously (Table 1), suggesting that Ti$_3$C$_2$/porous g-C$_3$N$_4$ photocatalyst is a promising photocatalytic system for H$_2$O$_2$ production.

To clarify the route of H$_2$O$_2$ production in the photocatalytic process, some control experiments were performed. As displayed in Fig. 7a, the H$_2$O$_2$ can hardly be examined in the absence of visible light irradiation, indicating that the H$_2$O$_2$ production is accomplished by photocatalysis. Moreover, no detectable amount of H$_2$O$_2$ is produced when O$_2$ is replaced by N$_2$, and the generation of H$_2$O$_2$ is suppressed in the absence of IPA. These results suggest that the H$_2$O$_2$ is mainly produced from the electron reduction of O$_2$ rather than the oxidation of H$_2$O by the photogenerated holes [8]. Fig. 7b shows the ESR spectra of DMPO-·O$_2^-$ adduct for the pCN and TC/pCN-2 samples. It is obvious can be seen that the DMPO-·O$_2^-$ adduct signal of TC/pCN-2 is much stronger than that of pCN under visible light irradiation, which is ascribed to the accelerated spatial charge separation and transfer, resulting in the enhanced intensity of DMPO-·O$_2^-$ adduct signal. The amount of ·O$_2^-$ formed in the photocatalysis is estimated by the NBT transformation method. As exhibited in Fig. S8, the intensity of characteristic absorption peak of NBT (260 nm) declines after photocatalytic

process. According to the reaction relationship between ·O$_2^-$ and NBT (4:1 in molar ratio), the average ·O$_2^-$ generation rates of pCN and TC/pCN-2 are evaluated to be 3.15 and 5.47 µmol L^{-1} h^{-1} (Fig. 7c). This result demonstrates the increased formation of ·O$_2^-$, which will further promote the production of H$_2$O$_2$.

To further investigate the pathway of O$_2$ reduction, rotating disk electrode (RDE) analysis of oxygen reduction reaction (ORR) were performed [67,68]. Fig. 7d and e depicts the linear sweep voltammetry (LSV) curves of pCN and TC/pCN-2 measured on a RDE in an O$_2$-saturated 0.1 mol L^{-1} phosphate buffer solution (pH 7) at different rotating speeds, respectively. The difference between Fig. 7d and e is not significant due to the limited content of Ti$_3$C$_2$, indicating that the loading of limited content of Ti$_3$C$_2$ has no obvious impact on the pathway of oxygen reduction reaction for porous g-C$_3$N$_4$. The Koutecky-Levich plots of the data at -1.0 V vs. Ag/AgCl are presented in Fig. 7f. The average number of electrons (n) involved in the overall reduction of O$_2$ is obtained by the linear regression of the plots using the following Eqs. (5) and (6):

$$j^{-1} = j_k^{-1} + B^{-1}\omega^{-1/2} \qquad (5)$$

$$B = 0.2nFv^{-1/6}CD^{2/3} \qquad (6)$$

Where j is the measured current density, j_k is the kinetic current density, ω is the rotating speed (rpm), F is the Faraday constant (96,485 C mol^{-1}), v is the kinetic viscosity of water (0.01 cm^2 s^{-1}), C is the bulk concentration of O$_2$ in water (1.26 × 10^{-3} mol cm^{-3}), and D is the diffusion coefficient of O$_2$ (2.7 × 10^{-5} cm^2 s^{-1}), respectively [69]. According to the intercept of the Koutecky-Levich plots, the j_k values of pCN and TC/pCN-2 are estimated to be 10.15 and 12.71 mA cm^{-2}, respectively, indicating that O$_2$ is reduced more efficiently on TC/pCN-2 [32]. The n values of pCN and TC/pCN-2 are 1.54 and 1.59, which are determined by the slope of the Koutecky-Levich plots. This result suggests that two-step single-electron O$_2$ reduction occurs on the pCN and TC/pCN-2, and the loading of Ti$_3$C$_2$ on g-C$_3$N$_4$ can promote the generation of electrons [11,34]. Therefore, The H$_2$O$_2$ production reaction in this photocatalytic process can be described as follows:

$$e^- + O_2 \rightarrow \bullet O_2^- \qquad (7)$$

$$\bullet O_2^- + e^- + 2H^+ \rightarrow H_2O_2 \qquad (8)$$

3.4. The mechanism of activity enhancement

The band gap energy (E_g) of pCN is determined to be 2.63 eV using Kubelka-Munk remission function (Fig. S9). Next, ultraviolet photoelectron spectroscopy (UPS) was employed to investigate the band
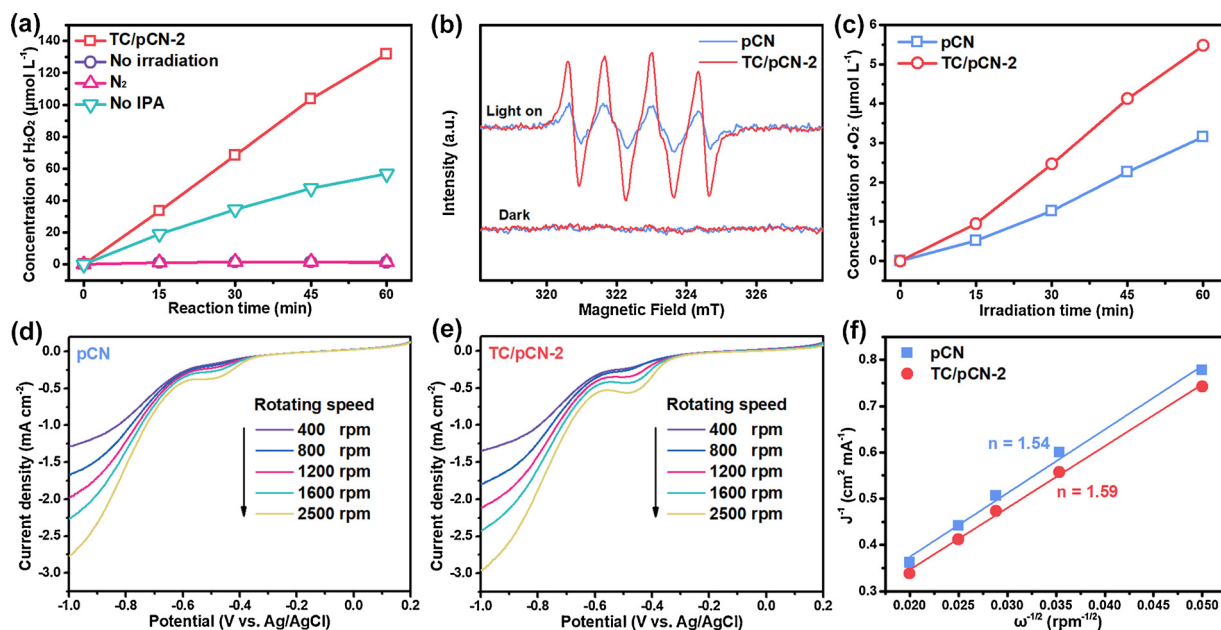
Fig. 7. (a) Comparison of the photocatalytic production of H_2O_2 under different conditions for TC/pCN-2; (b) ESR spectra of DMPO-$\cdot O_2^-$ adduct and (c) time-dependent concentration plots of $\cdot O_2^-$ for pCN and TC/pCN-2; LSV curves of (d) pCN and (e) TC/pCN-2 measured on a RDE at different rotating speeds; (f) Koutecky-Levich plots of the data obtained at the constant electrode potential (-1.0 V vs. Ag/AgCl).
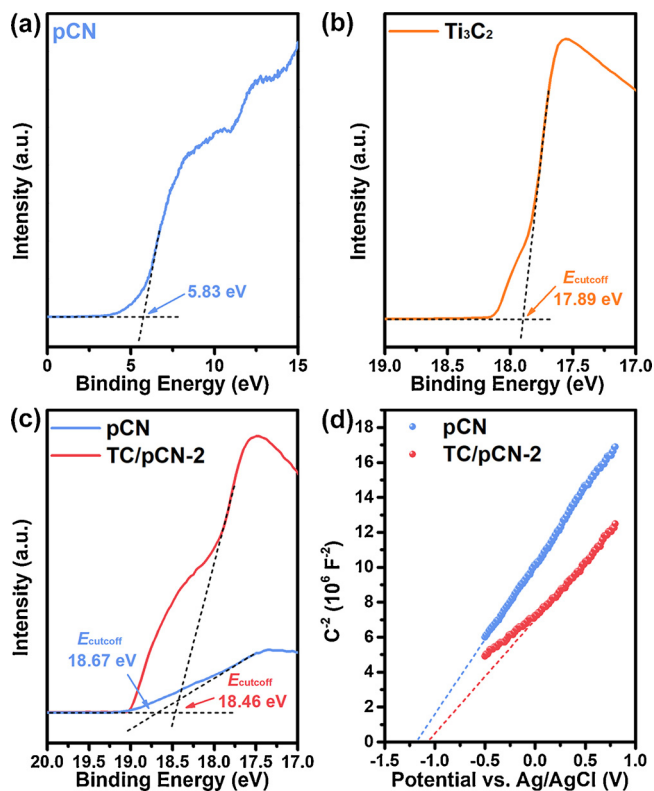

Fig. 8. UPS spectra of (a) pCN and (b) Ti_3C_2; (c) UPS spectra and (d) Mott-Schottky plots of pCN and TC/pCN-2.

structure of the samples. As shown in Fig. 8a, the valence band energy (E_{VB}) of pCN is determined to be 5.83 eV. And the conduction band energy (E_{CB}) is calculated to be 3.2 eV. Because the reference standard for which 0 V vs reversible hydrogen electrode (RHE) equals -4.44 eV vs vacuum level [70], the E_{VB} and E_{CB} of pCN can be estimated to be about 1.39 V and -1.24 V vs RHE, respectively. Moreover, the cutoff energy (E_{cutoff}) of Ti_3C_2, pCN and TC/pCN-2 are 17.89, 18.67 and 18.46 eV

(Fig. 8b and c), while their fermi level (E_f) are all 0 eV. Accordingly, their work functions ($e\Phi$) can be calculated to be 3.31, 2.53 and 2.74 eV according to the following equation, $e\Phi = h\nu - | E_{cutoff} - E_f |$ [71,72]. Obviously, the work function of Ti_3C_2 is greater than that of g-C_3N_4, thus a Schottky junction can be established after their contact. Such an upshift (0.21 eV) of the work function between pCN and TC/pCN-2 also verifies the existence of Schottky effect [71]. Besides, the slopes of the Mott-Schottky plots (Fig. 8d) demonstrate that porous g-C_3N_4 is n-type semiconductor and TC/pCN-2 presents larger carrier density owing the formation of Schottky junction.

On the basis of the above results, a possible photocatalytic mechanism over Ti_3C_2/porous g-C_3N_4 Schottky junction is proposed in Fig. 9. As mentioned above, the work functions of Ti_3C_2 ($e\Phi_{TC}$) and porous g-C_3N_4 ($e\Phi_{pCN}$) are determined to be 3.31 and 2.53 eV, respectively. When Ti_3C_2 and porous g-C_3N_4 are in contact, the visible-light induced electrons on porous g-C_3N_4 will flow to Ti_3C_2 at the lower energy level to achieve an equilibrium state between the fermi levels of Ti_3C_2 (E_{fTC}) and porous g-C_3N_4 (E_{fpCN}). A space charge layer thus can be generated on the side of porous g-C_3N_4, making the upward bending of energy band and inducing the formation of Schottky barrier (φ_{SB}). As a result, the electrons trapped by Ti_3C_2 can't flow back to conduction band (CB) of porous g-C_3N_4, which can highly efficient boost the spatial charge separation. Therefore, the Ti_3C_2 nanosheets can create a Schottky junction with the host porous g-C_3N_4 nanosheets to improve photocatalytic activity, and meanwhile, serve as the active sites for the H_2O_2 production.

4. Conclusion

Interfacial Schottky junction of Ti_3C_2 Mxene/porous g-C_3N_4 was designed and fabricated via the electrostatic self-assembly method. Benefitting from the Schottky effect and the accompanying built-in electric field, the photogenerated charges of porous g-C_3N_4 can be effectively separated and transferred. The TC/pCN-2 has the highest activity with an H_2O_2 production rate up to 2.20 μmol L^{-1} min^{-1} under visible light irradiation ($\lambda > 420$ nm). The mechanism analysis demonstrate that the two-step single-electron reduction of oxygen is the predominant reaction step during the photocatalytic H_2O_2 production process. This work promotes understanding of the mechanism of
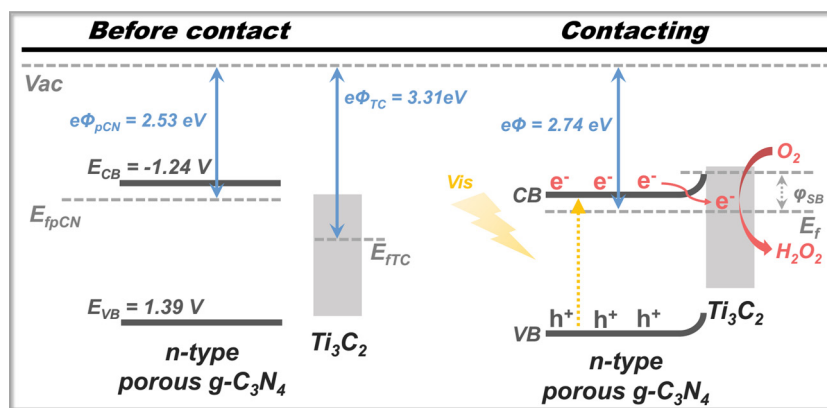
Fig. 9. The photocatalytic mechanism of the Ti_3C_2/porous g-C_3N_4 system.

photocatalytic H_2O_2 production and provides a new idea for the design and synthesis of new materials for the production of H_2O_2.

Appendix A. Supplementary data

Supplementary material related to this article can be found, in the online version, at doi:https://doi.org/10.1016/j.apcatb.2019.117956.

References

[1] Y. Wang, Y. Zhu, Y. Hu, G. Zeng, Y. Zhang, C. Zhang, C. Feng, Small (2018) 1703305.
[2] H. Yi, D. Huang, G. Zeng, C. Lai, L. Qin, M. Cheng, S. Ye, B. Song, X. Ren, X. Guo, Appl. Catal. B: Environ. 239 (2018) 408–424.
[3] J. Gong, B. Wang, G. Zeng, C. Yang, C. Niu, Q. Niu, W. Zhou, Y. Liang, J. Hazard. Mater. 164 (2009) 1517–1522.
[4] K. He, G. Chen, G. Zeng, A. Chen, Z. Huang, J. Shi, T. Huang, M. Peng, L. Hu, Appl. Catal. B: Environ. 228 (2018) 19–28.
[5] X. Tang, G. Zeng, C. Fan, M. Zhou, L. Tang, J. Zhu, J. Wan, D. Huang, M. Chen, P. Xu, Sci. Total Environ. 636 (2018) 1355.
[6] W. Xue, D. Huang, G. Zeng, J. Wan, C. Zhang, R. Xu, M. Cheng, R. Deng, J. Hazard. Mater. 341 (2018) 381–389.
[7] W. Xiong, Z. Zeng, G. Zeng, Z. Yang, R. Xiao, X. Li, J. Cao, C. Zhou, H. Chen, M. Jia, Y. Yang, W. Wang, X. Tang, Chem. Eng. J. 374 (2019) 91–99.
[8] Y. Zheng, Z. Yu, H. Ou, A.M. Asiri, Y. Chen, X. Wang, Adv. Funct. Mater. 28 (2018) 1705407.
[9] S. Zhao, T. Guo, X. Li, T. Xu, B. Yang, X. Zhao, Appl. Catal. B: Environ. 224 (2018) 725–732.
[10] M. Cheng, Y. Liu, D. Huang, C. Lai, G. Zeng, J. Huang, Z. Liu, C. Zhang, C. Zhou, L. Qin, W. Xiong, H. Yi, Y. Yang, Chem. Eng. J. 362 (2019) 865–876.
[11] S. Zhao, X. Zhao, J. Catal. 366 (2018) 98–106.
[12] S. Zhao, X. Zhao, Appl. Catal. B: Environ. 250 (2019) 408–418.
[13] W. Xiong, Z. Zeng, X. Li, G. Zeng, R. Xiao, Z. Yang, H. Xu, H. Chen, J. Cao, C. Zhou, L. Qin, Chemosphere 232 (2019) 186–194.
[14] S. Zhao, X. Zhao, H. Zhang, J. Li, Y. Zhu, Nano Energy 35 (2017) 405–414.
[15] L. Zhang, J. Zhang, G. Zeng, H. Dong, Y. Chen, C. Huang, Y. Zhu, R. Xu, Y. Cheng, K. Hou, Bioresour. Technol. 261 (2018) 10.
[16] S. Ye, G. Zeng, H. Wu, C. Zhang, J. Dai, J. Liang, J. Yu, X. Ren, H. Yi, M. Cheng, Crit. Rev. Biotechnol. 37 (2017) 1–15.
[17] P. Xu, G. Zeng, D. Huang, C. Feng, S. Hu, M. Zhao, C. Lai, Z. Wei, C. Huang, G. Xie, Sci. Total Environ. 424 (2012) 1–10.
[18] L. Qin, G. Zeng, C. Lai, D. Huang, C. Zhang, P. Xu, T. Hu, X. Liu, M. Cheng, Y. Liu, L. Hu, Y. Zhou, Sens. Actuators B: Chem. 243 (2017) 946–954.
[19] C. Zhang, W. Wang, A. Duan, G. Zeng, D. Huang, C. Lai, X. Tan, M. Cheng, R. Wang, C. Zhou, W. Xiong, Y. Yang, Chemosphere 222 (2019) 184–194.
[20] C. Zhang, G. Zeng, D. Huang, C. Lai, M. Chen, M. Cheng, W. Tang, L. Tang, H. Dong, B. Huang, X. Tan, R. Wang, Chem. Eng. J. 373 (2019) 902–922.
[21] L. Li, C. Lai, F. Huang, M. Cheng, G. Zeng, D. Huang, B. Li, S. Liu, M. Zhang, L. Qin, M. Li, J. He, Y. Zhang, L. Chen, Water Res. 160 (2019) 238–248.
[22] Y. Yang, C. Zhang, C. Lai, G. Zeng, D. Huang, M. Cheng, J. Wang, F. Chen, C. Zhou, W. Xiong, Adv. Colloid Interface Sci. 254 (2018) 76–93.
[23] H. Wang, Z. Zeng, P. Xu, L. Li, G. Zeng, R. Xiao, Z. Tang, D. Huang, L. Tang, C. Lai, D. Jiang, Y. Liu, H. Yi, L. Qin, S. Ye, X. Ren, W. Tang, Chem. Soc. Rev. 48 (2019) 488–516.
[24] J. Cao, Z. Yang, W. Xiong, Y. Zhou, Y. Peng, X. Li, C. Zhou, R. Xu, Y. Zhang, Chem. Eng. J. 353 (2018) 126–137.
[25] X. Li, P. Xu, M. Chen, G. Zeng, D. Wang, F. Chen, W. Tang, C. Chen, C. Zhang, X. Tan, Chem. Eng. J. 366 (2019) 339–357.
[26] D. Huang, Z. Li, G. Zeng, C. Zhou, W. Xue, X. Gong, X. Yan, S. Chen, W. Wang, M. Cheng, Appl. Catal. B: Environ. 240 (2019) 153–173.
[27] D. Huang, S. Chen, G. Zeng, X. Gong, C. Zhou, M. Cheng, W. Xue, X. Yan, J. Li, Coord. Chem. Rev. 385 (2019) 44–80.
[28] G. Liao, Y. Gong, L. Zhang, H. Gao, G. Yang, B. Fang, Energy Environ. Sci. 12 (2019) 2080–2147.
[29] Y. Shiraishi, S. Kanazawa, Y. Sugano, D. Tsukamoto, H. Sakamoto, S. Ichikawa, T. Hirai, ACS Catal. 4 (2014) 774–780.
[30] Z. Wei, M. Liu, Z. Zhang, W. Yao, H. Tan, Y. Zhu, Energy Environ. Sci. 11 (2018) 2581–2589.
[31] J. Cai, J. Huang, S. Wang, J. Iocozzia, Z. Sun, J. Sun, Y. Yang, Y. Lai, Z. Lin, Adv. Mater. (2019) e1806314.
[32] Y. Shiraishi, Y. Kofuji, H. Sakamoto, S. Tanaka, S. Ichikawa, T. Hirai, ACS Catal. 5 (2015) 3058–3066.
[33] L. Shi, L. Yang, W. Zhou, Y. Liu, L. Yin, X. Hai, H. Song, J. Ye, Small 14 (2018) 1703142.
[34] S. Li, G. Dong, R. Hailili, L. Yang, Y. Li, F. Wang, Y. Zeng, C. Wang, Appl. Catal. B: Environ. 190 (2016) 26–35.
[35] G.-h. Moon, M. Fujitsuka, S. Kim, T. Majima, X. Wang, W. Choi, ACS Catal. 7 (2017) 2886–2895.
[36] Y. Shiraishi, S. Kanazawa, Y. Kofuji, H. Sakamoto, S. Ichikawa, S. Tanaka, T. Hirai, Angew. Chem. Int. Ed. 53 (2014) 13454–13459.
[37] Y. Kofuji, Y. Isobe, Y. Shiraishi, H. Sakamoto, S. Tanaka, S. Ichikawa, T. Hirai, J. Am. Chem. Soc. 138 (2016) 10019–10025.
[38] M. Naguib, O. Mashtalir, J. Carle, V. Presser, J. Lu, L. Hultman, Y. Gogotsi, M.W. Barsoum, ACS Nano 6 (2012) 1322.
[39] H. Wang, Y. Wu, X. Yuan, G. Zeng, J. Zhou, X. Wang, J.W. Chew, Adv. Mater. 30 (2018) e1704561.
[40] Y. Xu, S. Wang, J. Yang, B. Han, R. Nie, J. Wang, Y. Dong, X. Yu, J. Wang, H. Jing, J. Mater. Chem. A 6 (2018) 15213–15220.
[41] T. Cai, L. Wang, Y. Liu, S. Zhang, W. Dong, H. Chen, X. Yi, J. Yuan, X. Xia, C. Liu, S. Luo, Appl. Catal. B: Environ. 239 (2018) 545–554.
[42] H. Wang, Y. Sun, Y. Wu, W. Tu, S. Wu, X. Yuan, G. Zeng, Z.J. Xu, S. Li, J.W. Chew, Appl. Catal. B: Environ. 245 (2019) 290–301.
[43] J. Ran, G. Gao, F. Li, T. Ma, A. Du, S. Qiao, Nat. Commun. 8 (2017) 13907.
[44] S. Cao, B. Shen, T. Tong, J. Fu, J. Yu, Adv. Funct. Mater. 28 (2018) 1800136.
[45] C. Zhou, S. Wang, Z. Zhao, Z. Shi, S. Yan, Z. Zou, Adv. Funct. Mater. 28 (2018) 1801214.
[46] H. Zhong, C. Yang, L. Fan, Z. Fu, X. Yang, X. Wang, R. Wang, Energy Environ. Sci. 12 (2019) 418–426.
[47] X. She, H. Xu, Y. Yu, L. Li, X. Zhu, Z. Mo, Y. Song, J. Wu, S. Yuan, H. Li, Small 15 (2019) e1804613.
[48] Y. Sun, D. Jin, Y. Sun, X. Meng, Y. Gao, Y. Dall'Agnese, G. Chen, X. Wang, J. Mater. Chem. A 6 (2018) 9124–9131.
[49] J. Xuan, Z. Wang, Y. Chen, D. Liang, L. Cheng, X. Yang, Z. Liu, R. Ma, T. Sasaki, F. Geng, Angew. Chem. Int. Ed. 128 (2016) 14789–14794.
[50] C. Zhou, C. Lai, D. Huang, G. Zeng, C. Zhang, M. Cheng, L. Hu, J. Wan, W. Xiong, M. Wen, X. Wen, L. Qin, Appl. Catal. B: Environ. 220 (2018) 202–210.

[51] Y. Yang, C. Zhang, D. Huang, G. Zeng, J. Huang, C. Lai, C. Zhou, W. Wang, H. Guo, W. Xue, R. Deng, M. Cheng, W. Xiong, Appl. Catal. B: Environ. 245 (2019) 87–99.

[52] W. Wang, Z. Zeng, G. Zeng, C. Zhang, R. Xiao, C. Zhou, W. Xiong, Y. Yang, L. Lei, Y. Liu, Chem. Eng. J. 15 (2019) 122132.

[53] C. Zhou, P. Xu, C. Lai, C. Zhang, G. Zeng, D. Huang, M. Cheng, L. Hu, W. Xiong, X. Wen, L. Qin, J. Yuan, W. Wang, Chem. Eng. J. 359 (2019) 186–196.

[54] W. Wang, P. Xu, M. Chen, G. Zeng, C. Zhang, C. Zhou, Y. Yang, D. Huang, C. Lai, M. Cheng, L. Hu, W. Xiong, H. Guo, M. Zhou, ACS Sustain. Chem. Eng. 6 (2018) 15503–15516.

[55] L. Qin, D. Huang, P. Xu, G. Zeng, C. Lai, Y. Fu, H. Yi, B. Li, C. Zhang, M. Cheng, J. Colloid Interface Sci. 534 (2019) 357–369.

[56] C. Zhou, D. Huang, P. Xu, G. Zeng, J. Huang, T. Shi, C. Lai, C. Zhang, M. Cheng, Y. Lu, Chem. Eng. J. 370 (2019) 1077–1086.

[57] H. Guo, C. Niu, D. Huang, N. Tang, C. Liang, L. Zhang, X. Wen, Y. Yang, W. Wang, G. Zeng, Chem. Eng. J. 360 (2019) 349–363.

[58] Y. Lin, S. Wu, C. Yang, M. Chen, X. Li, Appl. Catal. B: Environ. 245 (2019) 71–86.

[59] W. Xue, Z. Peng, D. Huang, G. Zeng, X. Wen, R. Deng, Y. Yang, X. Yan, Ceram. Int. 45 (2019) 6340–6349.

[60] H. Guo, H. Niu, C. Liang, C. Niu, D. Huang, L. Zhang, N. Tang, Y. Yang, C. Feng, G. Zeng, J. Catal. 370 (2019) 289–303.

[61] B. Li, C. Lai, G. Zeng, L. Qin, H. Yi, D. Huang, C. Zhou, X. Liu, M. Cheng, P. Xu, C. Zhang, F. Huang, S. Liu, ACS Appl. Mater. Interface 10 (2018) 18824–18836.

[62] H. Yi, M. Yan, D. Huang, G. Zeng, C. Lai, M. Li, X. Huo, L. Qin, S. Liu, X. Liu, B. Li, H. Wang, M. Shen, Y. Fu, X. Guo, Appl. Catal. B: Environ. 250 (2019) 52–62.

[63] S. Ye, M. Yan, X. Tan, J. Liang, G. Zeng, H. Wu, B. Song, C. Zhou, Y. Yang, H. Wang, Appl. Catal. B: Environ. 250 (2019) 78–88.

[64] Y. Lin, S. Wu, X. Li, X. Wu, C. Yang, G. Zeng, Y. Peng, Q. Zhou, L. Lu, Appl. Catal. B: Environ. 227 (2018) 557–570.

[65] Y. Yang, Z. Zeng, C. Zhang, D. Huang, G. Zeng, R. Xiao, C. Lai, C. Zhou, H. Guo, W. Xue, M. Cheng, W. Wang, J. Wang, Chem. Eng. J. 349 (2018) 808–821.

[66] H.I. Kim, O.S. Kwon, S. Kim, W. Choi, J.H. Kim, Energy Environ. Sci. 9 (2016) 1063–1073.

[67] C. Zhang, C. Lai, G. Zeng, D. Huang, L. Tang, C. Yang, Y. Zhou, L. Qin, M. Cheng, Biosens. Bioelectron. 81 (2016) 61–67.

[68] C. Lai, S. Liu, C. Zhang, G. Zeng, D. Huang, L. Qin, X. Liu, H. Yi, R. Wang, F. Huang, ACS Sens. 3 (2018) 2566–2573.

[69] Y. Liu, H. Liu, C. Wang, S. Hou, N. Yang, Environ. Sci. Technol. 47 (2013) 13889–13895.

[70] X. She, J. Wu, H. Xu, J. Zhong, Y. Wang, Y. Song, K. Nie, Y. Liu, Y. Yang, M.-T.F. Rodrigues, R. Vajtai, J. Lou, D. Du, H. Li, P.M. Ajayan, Adv. Energy Mater. 7 (2017) 1700025.

[71] Z. Zhuang, Y. Li, Z. Li, F. Lv, Z. Lang, K. Zhao, L. Zhou, L. Moskaleva, S. Guo, L. Mai, Angew. Chemie Int. Ed. 57 (2018) 496–500.

[72] Z. Li, Z. Zhuang, F. Lv, H. Zhu, L. Zhou, M. Luo, J. Zhu, Z. Lang, S. Feng, W. Chen, Adv. Mater. 30 (2018) 1803220.